

TABLE I. The SLy EOS. In the first column are the dividing rest-mass densities in g/cm^3 , while in the second column are the polytropic indices.

ρ_{0i}	Γ_i
-	2.85100
1.00000×10^{15}	2.98800
5.01187×10^{14}	3.00500
1.46220×10^{14}	1.35692

constant angular momentum and constant rest mass are constructed and stability questions are addressed.

II. NUMERICAL METHODS

Our equilibria are constructed with the Cook-Shapiro-Teukolsky (CST) code [20], which solves the Einstein equations for rotating equilibria under the assumptions of stationarity and axisymmetry. The spacetime element (units of $G = c = 1$) is in the form of

$$ds^2 = -e^{\gamma+\rho} dt^2 + e^{2\alpha} (dr^2 + r^2 d\theta^2) + e^{\gamma-\rho} r^2 \sin^2 \theta (d\phi - \omega dt)^2, \quad (1)$$

where $\gamma, \rho, \alpha, \omega$ are all functions of r and θ only, while the stress-energy tensor is written as

$$T_{\mu\nu} = (\rho_0 + \rho_i + P)u_\mu u_\nu + P g_{\mu\nu}, \quad (2)$$

where ρ_0 is the rest-mass density, ρ_i the internal energy density, and P the pressure at the rest frame of the fluid. Here, u^μ is the fluid four-velocity that for a circular flow considered here may be written as $u^\mu = u^t (t^\mu + \Omega \phi^\mu)$, where t^μ is the timelike Killing vector that defines stationarity, and ϕ^μ is the azimuthal spacelike Killing vector that defines axisymmetry. The angular velocity Ω is constant for uniform rotation but a function of r and θ when differential rotation is considered. The vanishing divergence of the stress-energy tensor, together with the assumptions of stationarity and axisymmetry, lead to the Euler equation of hydrostatic equilibrium [20]. In the case of uniform rotation, the Euler equation can be directly integrated, while in the case of differential rotation, it can be integrated when the specific angular momentum $j = u^t u_\phi$ is a function of Ω itself [20, 22]. In this work, we will consider either uniform rotation or differential rotation described by the Komatsu-Eriguchi-Hachisu law [9, 23] $j(\Omega) = A^2(\Omega_c - \Omega)$, where Ω_c is the angular velocity at the center of the star, and A is a parameter that controls the amount of differential rotation. To probe for the existence of the ergosphere, we examine at every point the sign of the norm of the vector t^μ , and in particular, we identify where the condition

$$\mathbf{t} \cdot \mathbf{t} = g_{tt} = e^{\gamma-\rho} (\omega^2 r^2 \sin^2 \theta - e^{2\rho}) > 0 \quad (3)$$

is satisfied.

The first EOS that we consider here uses the SLy EOS [21] in the form of a piecewise representation $P = K_i \rho_0^{\Gamma_i}$

TABLE II. The four EOSs employed here. The columns are the maximum spherical mass $M_{\text{max}}^{\text{TOV}}$ in units of M_\odot , the maximum mass of the uniformly rotating models $M_{\text{max}}^{\text{Kep}}$, and the corresponding rest-mass densities in g/cm^3 .

EOS	$M_{\text{max}}^{\text{TOV}}$	$M_{\text{max}}^{\text{Kep}}$	$\rho_{0\text{max}}^{\text{TOV}}$	$\rho_{0\text{max}}^{\text{Kep}}$
SLy	2.061	2.488	1.999×10^{15}	1.771×10^{15}
SLycc1	4.067	5.280	5.979×10^{14}	5.175×10^{14}
SLycc2	2.917	3.656	1.139×10^{15}	1.022×10^{15}
SLycc4	2.222	2.681	1.852×10^{15}	1.721×10^{15}

[24]. The matching rest-mass densities ρ_{0i} as well as the polytropic indices Γ_i are shown in Table I. A polytropic constant is calculated from the reference values of pressure ($2.42103 \times 10^{34} \text{ dyn}/\text{cm}^2$) and density ($5.01187 \times 10^{14} \text{ g}/\text{cm}^3$), while the rest of the polytropic constants are calculated from the equality of pressure at the dividing densities of Table I. The other three EOSs (SLycc1, SLycc2, and SLycc4) are based on the SLy one where we progressively substitute an inner core at matching densities $\rho_{0\text{nuc}}, 2\rho_{0\text{nuc}},$ and $4\rho_{0\text{nuc}}$, with the maximally stiff EOS [25]

$$P = \sigma(\epsilon - \epsilon_s) + P_s. \quad (4)$$

Here, σ is a dimensionless parameter, $\epsilon = \rho_0 + \rho_i$ is the total energy density, and P_s the pressure at ϵ_s . The solutions presented in this work assume $\sigma = 1.0$, i.e., a core at the causal limit, which represents the compressible EOS that yields configurations of maximal compactness [26]. Equation (4) relates the pressure to the total energy density when $\rho_0 \geq \rho_{0s} = \rho_{0\text{nuc}}, 2\rho_{0\text{nuc}}, 4\rho_{0\text{nuc}}$ for the SLycc1, SLycc2, and SLycc4 EOSs respectively, while for $\rho_0 \leq \rho_{0s}$ the SLy EOS is recovered. One can express the pressure in terms of the rest-mass density in a polytropic form by integrating the first law of the thermodynamics $d\epsilon/(\epsilon + P) = d\rho_0/\rho_0$. Using Eq. (4), we get for $\rho_0 \geq \rho_{0s}$,

$$P = \frac{1}{\sigma + 1} (\sigma \kappa \rho_0^{\sigma+1} + P_s - \sigma \epsilon_s), \quad (5)$$

$$\epsilon = \frac{1}{\sigma + 1} (\kappa \rho_0^{\sigma+1} + \sigma \epsilon_s - P_s), \quad (6)$$

$$h = \kappa \rho_0^\sigma, \quad (7)$$

where the constant $\kappa = h_s / \rho_{0s}^\sigma$, and $h = (\rho_0 + \rho_i + P) / \rho_0$ is the specific enthalpy. The value h_s can be evaluated from the polytrope outside the core.

III. RESULTS

For the four EOSs described above the maximum spherical mass $M_{\text{max}}^{\text{TOV}}$, the maximum mass at the mass-shedding limit under uniform rotation $M_{\text{max}}^{\text{Kep}}$, as well as their corresponding rest-mass densities are shown in Table II. We note here that the SLy EOS has a speed of sound $c_s = \sqrt{dP/d\epsilon}$ larger than the speed of light when $\rho_0 \geq 1.999 \times 10^{15} \text{ g}/\text{cm}^3$ which is identical to the density at the maximum mass. For the other

three EOSs, since $4\rho_{0\text{nuc}}$ is less than this value, we always have $c_s \leq c$.

Figure 1 is devoted to the SLy EOS. The top and middle rows depict the position of ergostars (green crosses) in a mass vs central rest-mass density diagram.¹ Every panel corresponds to a different degree of differential rotation starting from uniform rotation in the top left panel where $\hat{A}^{-1} = 0$ and progressing to a higher degree of differential rotation in the right middle panel where $\hat{A}^{-1} = 1$. In each plot, we show the spherical solutions (TOV black curve), the mass-shedding limit of uniformly rotating stars (red curve), sequences of constant rest mass M_0 (orange dashed curves), sequences of constant angular momentum J (brown dashed curves), and the curve that joins the maximum mass points (turning points) on every $J = \text{const}$ sequence (blue dashed curve). In a typical calculation, for every \hat{A} (i.e., for every panel) we divide a range of densities starting from a low density up to the limiting point $2.0 \times 10^{15} \text{ g/cm}^3$ into 60 intervals, and using the CST code we compute 60 constant rest-mass density sequences from the spherical limit (black curve) all the way up into more massive models that have small ratios R_p/R_e until the code fails to converge. Here, R_p is the polar radius. The last points, i.e., the points with the smaller value of R_p/R_e , on every sequence are connected with a dashed red curve in the panels of the top and middle row in Fig. 1. As we can see, there are no ergostars for uniformly rotating models or small differential rotation $\hat{A}^{-1} = 0.2$ for the SLy EOS. On the other hand, the largest number of ergostars appear when \hat{A}^{-1} is approximately in the range $0.4 - 0.6$, while for larger degrees of differential rotation, they tend to diminish again.

One important line in these plots is the blue dashed line which separates the secularly unstable/stable models against axisymmetric perturbations. For the uniformly rotating case, it is denoted as the turning point line due to “turning point theorem” of Friedman, *et al.* [27]: Along a sequence of uniformly rotating stars with fixed angular momentum and increasing central density, the configuration of maximum mass marks the onset of *secular* instability. The turning point line is also commonly taken to be the criterion for distinguishing *dynamical* stability. Although the analysis of Takami *et al.* [28] implies that the loci of secular, dynamical, and turning point lines is more subtle, they clearly are close to each other. For differential rotation, there is no analogous theorem, but there is significant evidence that again the locus of dynamical stability is very close to the turning point on $J = \text{const}$ curves [29–31]. According to [28, 31], the dynamical instability typically sets in at central densities slightly below the one that corresponds to the turning point. In particular, as one moves along a $J = \text{const}$ sequence toward increasing densities, one encounters the secular instability first, then the dynamical, and finally the turning point. Given that all three points are very close together and given the lack of any general theorem, we will assume here that the turning points mark the beginning of

the dynamically unstable region, although the reader should be aware of the differences discussed above. We also note here that in the cases with differential rotation, the CST code can go to large deformations (i.e., small ratios of R_p/R_e) that correspond to toroidal configurations. On the other, hand in some cases, especially for large masses and smaller densities, we were not able to find a turning point. Typically, for those cases a fixed angular momentum sequence is a monotonically increasing function of mass as one moves to larger densities. For our present purposes, we tacitly assume that the last points in those sequences signify the dynamical instability limit, although in reality that limit should be on the left at higher densities.²

This implies that *all ergostars on and to the right of the blue dashed lines are dynamically unstable*. For the SLy EOS, Fig. 1, this criterion rules out most of the ergostars, at least for a mild degree of differential rotation ($\hat{A}^{-1} = 0.4, 0.6$). For larger differential rotation, the ergostars tend to accumulate close to the turning point line (or more precisely, close to the last model we were able to calculate), and given the discussion above, the dynamical stability of these models is questionable, as a full evolution will be needed for a diagnosis. We also note here that as differential rotation becomes larger, the turning point line becomes straighter and rotates counter-clockwise with respect to the maximum spherical point. This also implies that *all models on and to the right of the uniformly rotating turning point line are dynamically unstable irrespective of the degree of differential rotation*. In addition, this is true for supramassive as well as hypermassive stars.

To get a better understanding of the qualitative features of the SLy ergostars, we plot in the bottom row of Fig. 1 the deformation parameter R_p/R_e as well as the rotational kinetic over the gravitational potential energy T/W for three representative cases of differential rotation. The vertical black line corresponds to the density of the maximum spherical mass, while the red one corresponds to the density of the maximum uniformly rotating mass. We find that all models with $\hat{A}^{-1} = 0.4, 0.6, 0.8$ are toroidal (i.e., the maximum density is not at the center), and the larger the differential rotation, the more toroidal shapes we were able to compute. Note that according to recent studies [34], extreme toroidal configurations are dynamically unstable. In the T/W panels, we draw with a horizontal dashed-dot line the $T/W = 0.25$ benchmark, which in many cases provides a crude criterion for the onset of dynamical instability to nonaxisymmetric (bar) modes [35, 36]. Blue crosses correspond to ergostars on the left of the turning point line, while red crosses correspond to ergostars on the right of the turning point line.

Figure 2 is similar to Fig. 1, but it corresponds to the SLycc1 EOS. The effect of the large causal core is immediately seen even for the uniformly rotating models: Supramassive ergostars now appear, but they all lie in the dynamical unstable part of the parameter space. We also note here that the

¹ Here we use the notation of the CST code [20] where $\hat{A} = A/R_e$, R_e being the equatorial radius.

² It is possible that more fine-tuned codes like [32, 33] can go beyond our calculated models and refine the position of the turning point in the very high mass differentially rotating regime.

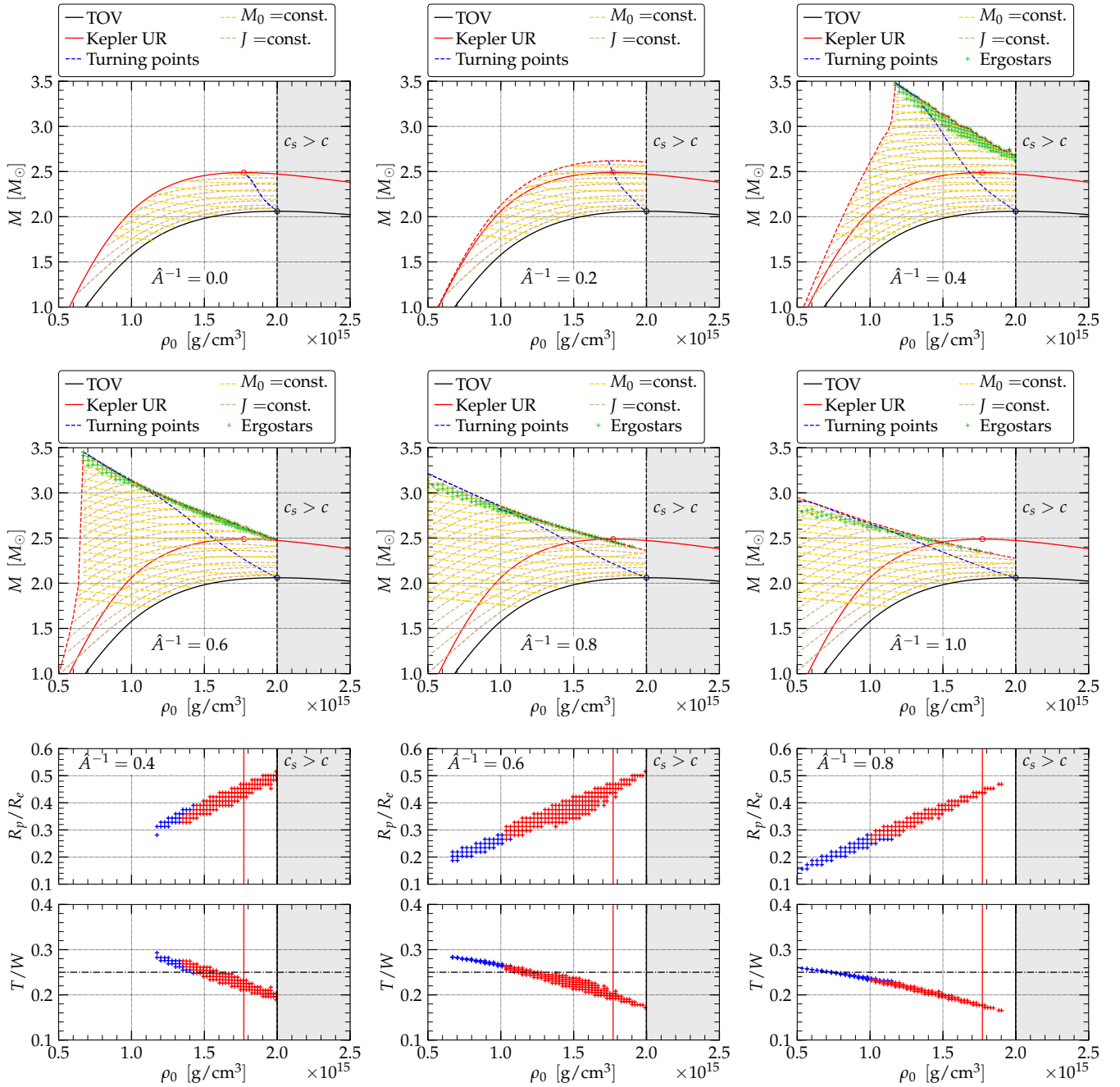


FIG. 1. SLy EOS. Top and middle row depict the location of the ergostars (green cross) in a mass vs central rest-mass density diagrams for different degrees of differential rotation \hat{A} . The panel with $\hat{A}^{-1} = 0$ (top left) corresponds to uniform rotation. Bottom row shows the deformation (R_p/R_e) and T/W for three differential rotation cases. Blue crosses correspond to ergostars on the left of the turning point line, while red crosses correspond to the ones on the right.

maximum mass of the spherical solutions, as well as the maximum mass at the mass-shedding limit, increase considerably from the SLy EOS (by factors of 1.97 and 2.12, respectively). This has already been seen with the ALF2cc EOS employed in [8, 37]. Given the fact that the SLycc1 and ALF2cc EOSs only differ in the crust (i.e., for $\rho_0 \leq \rho_{0\text{nuc}}$), it is not surprising that the differences in the TOV and Kepler lines are minute.

In addition, comparing SLycc1 vs SLy, we see that the densities where the maximum mass for the spherical and mass-shedding sequence reduce significantly (by factors of 3.34 and 3.42, respectively; see Table II). Although this may seem contradictory, it is related to the fact that the density profile along an axis is quite different from models using a typical EOS (like SLy or ALF2) without a large causal core. Instead of a

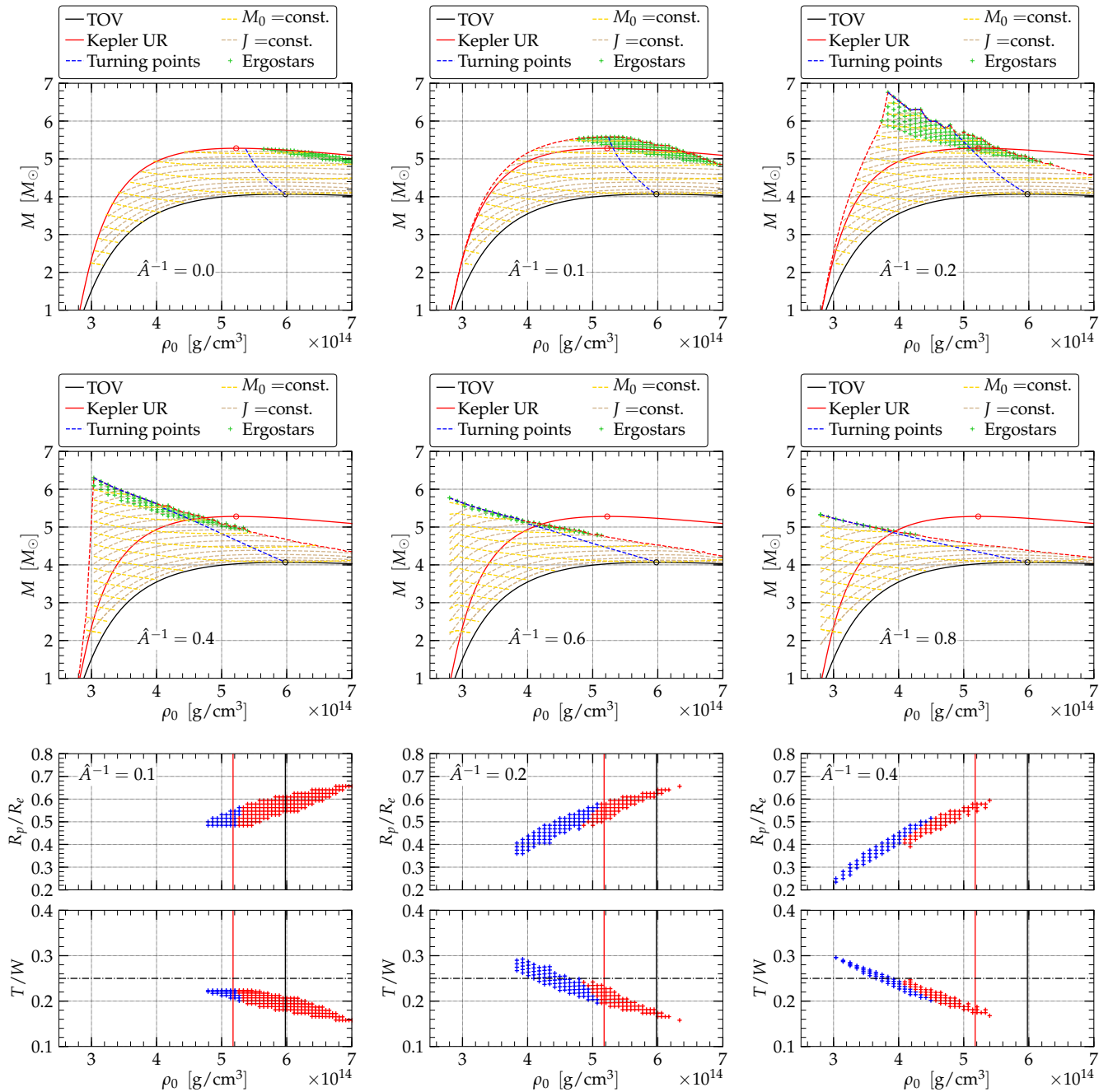


FIG. 2. Same as Fig. 1 but for the SLycc1 EOS.

parabolic type, the profile with SLycc1 starts from a smaller central density, diminishes somewhat all the way to the surface of the star, where it abruptly reduces to zero (see Fig. 1 in [37]). In this respect, stars with the SLycc1 or ALF2cc EOS resemble quark stars that have a finite surface density.

When differential rotation is considered, the general trends are (1) the turning point line moves up and turns counterclockwise with respect to the maximum TOV mass point, as in Fig. 1. (2) The ergostars move toward smaller densities well beyond the turning point line, toward the stable part of the pa-

rameter space. (3) For a larger degree of differential rotation, the ergostars tend to accumulate toward the turning point line and also the number of them tends to decrease. When differential rotation is large enough, the ergostars almost disappear.

The fact that a very mild differential rotation moved the ergostars from the unstable regime at high densities on the right of the turning point line to the left at lower central densities enabled us to find dynamically stable models [8]. Although these models used a different EOS (ALF2cc), they do not differ significantly from the models of Fig. 2 since apart

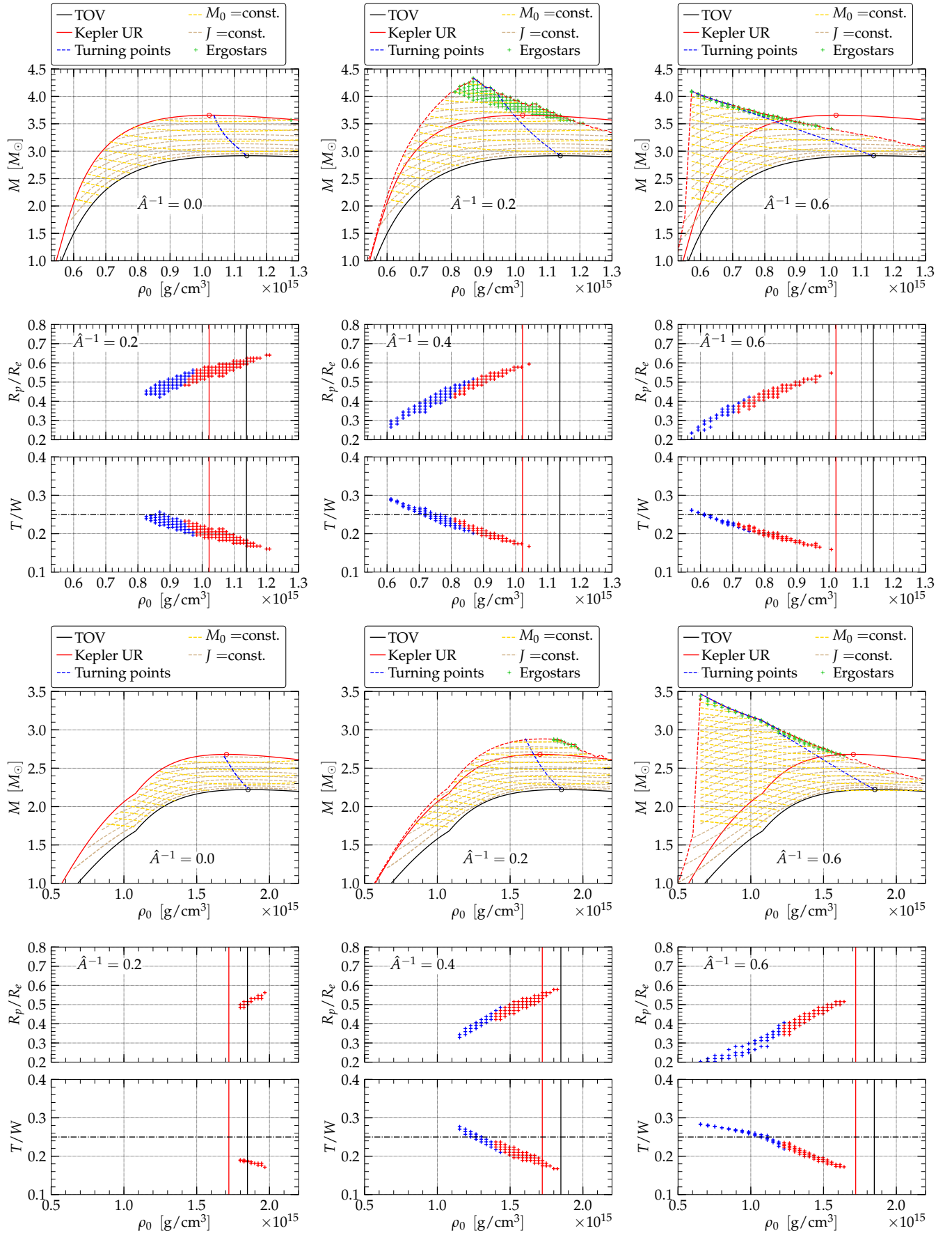


FIG. 3. Same as Fig. 1 but for the SLycc2 (first and second rows) and SLycc4 (third and fourth rows) EOSs.

from a small crust, the rest of the star has the same (causal) EOS. In particular, the featured model in Fig. 1 of [8] had $\hat{A}^{-1} = 0.2$, a central density $\rho_0 = 4.52 \times 10^{14} \text{ g/cm}^3$, and mass $M = 5.709 M_\odot$. Looking at the right panel of the top row in Fig. 2, we can see that indeed such a model lies within the dynamically stable regime.

From the bottom row panels of Fig. 2, where differential rotation is small ($\hat{A}^{-1} = 0.1$) all ergostars are spheroidal for the SLycc1 EOS, and they progressively become toroidal with higher differential rotation (this is in contrast with the SLy EOS where almost all ergostars found had toroidal topology). Also, T/W for the spheroidal models is below the benchmark value of 0.25, while it becomes larger and reaches the 0.3 value as differential rotation is increased. We note here that for $\hat{A}^{-1} = 0.1$, the ergostars to the right of the blue line (which are the majority of them) should be unstable to axisymmetric perturbations. For the small number of ergostars to the left of the red line the possibility of dynamical stability is significant. For $\hat{A}^{-1} = 0.2$, all models with density larger than approximately $\rho_0 \approx 5 \times 10^{14} \text{ g/cm}^3$ should also be unstable to axisymmetric perturbations, but the ones with less central density can be stable even with respect to nonaxisymmetric modes (there are many models with $T/W < 0.25$ and even some with $T/W > 0.25$ can be stable). Similar arguments can be made for $\hat{A}^{-1} = 0.4$.

When the causal core is assumed at $2\rho_{0\text{nuc}}$, ergostars almost disappear from the uniformly rotating regime (Fig. 3 top left panel). Similar to the SLycc1 EOS, small differential rotation ($\hat{A}^{-1} = 0.2$) brings ergostars into the stable side of the turning point line and, according to Fig. 3 second row left panel, these are possibly stable against nonaxisymmetric perturbations. As the degree of differential rotation increases, the turning point line turns counterclockwise with respect to the maximum spherical mass point, and the ergostars accumulate toward the end point of our convergence regime. The middle and right panels in the second row of Fig. 3 show the deformation and T/W when $\hat{A}^{-1} = 0.4, 0.6$ for the SLycc2 EOS. Full simulations will be needed to probe the fate of these equilibria. The bottom two rows in Fig. 3 depict the ergostars when the causal core shifts at $4\rho_{0\text{nuc}}$. Here, the EOS is very close to the original SLy, apart from the very high density regime; thus, the position of the ergostars resembles the one found in Fig. 1.

IV. DISCUSSION

It has recently been proposed [5, 6] that the mechanism behind the launching of relativistic jets from compact objects is the ergosphere and not a black hole horizon. In [7], the authors tested a simplified version of this scenario by performing a force-free numerical simulation of a homogeneous ergostar using the Cowling approximation. They confirmed that the Blandford-Znajek mechanism is not directly related to the horizon of the black hole by showing that (a) the magnetic field collimation, (b) the induced charged density and poloidal currents, and (c) the electromagnetic luminosity that

are produced by a rotating ergostar are similar to those observed in a rotating black hole spacetime. Their use of an incompressible EOS together with their freezing of the gravitational field, raises doubts regarding the stability of ergostars in a realistic evolutionary scenario. As in [38–40], we define an incipient jet based on the following three characteristics: (1) a collimated, tightly wound magnetic field, (2) a mildly relativistic outflow ($\Gamma_L > 1.2$), and (3) the outflow is confined by a funnel containing a (nearly) force-free magnetic field $b^2/(2\rho_0) > 1$. Here, $b^2 = B^2/(4\pi)$, and B is the magnetic field at the poles. In the case of [7], the absence of all matter does not permit conditions (2) and (3) to be checked, which motivates our efforts to explore the parameter space of dynamically stable ergostars with a compressible and causal EOS.

Regarding the Friedman instability, it was shown that the $m = 2$ bar mode of a homogeneous ergostar having a period $T = 27M$ has a growth time $\tau_F \approx 10^8 M$ [13]. Larger values of m have even larger τ_F . On the other hand, the Alfvén timescale is

$$\frac{\tau_A}{M} = \frac{\sqrt{4\pi\epsilon}}{B} \left(\frac{R}{M} \right). \quad (8)$$

For typical ergostars and $B \sim 10^{12} \text{ G}$, one gets $\tau_A/M \sim 10^6 \sim \tau_F/100$. Therefore, it is improbable that the Friedman instability will have any effect on the possible formation of a jet. On the other hand, large magnetic fields ($\gtrsim 10^{15} \text{ G}$) are needed to bring the Alfvén timescale on levels that can be currently simulated ($\lesssim 10^3 M$) but sufficiently small that they are not dynamically significant initially.

In this work, we constructed more than $\sim 30,000$ uniformly and differentially rotating equilibria using four EOSs in order to probe the parameter space and identify the parameters under which ergostars appear. The most favorable parameters will be adopted in the future for full magnetohydrodynamical simulations. Using the SLy EOS as a basis, we constructed three other EOSs by imposing a causal core at $\rho_{0\text{nuc}}, 2\rho_{0\text{nuc}}$, and $4\rho_{0\text{nuc}}$. We expect that similar behavior will be found when any other EOS is used instead of the SLy one. The differential rotation law that we explored is the so-called “ j -const” law, and it will be interesting in the future to see how robust our findings are when other differential rotating laws are employed, like those presented in [41] that model more accurately the rotation profile of a neutron star merger remnant. In all cases considered, we calculated the turning point line [27] and commented on the stability properties of the ergostars that we found. For a regular EOS like the SLy, most ergostars appear on the unstable side of the turning point line, but for small differential rotation, models on the stable side also appear. These stars typically are highly hypermassive and very close to the limits of convergence for the CST code. Their stability will have to be probed by full general relativistic simulations as in [8]. For an EOS like SLycc1, ergostars appear more frequently for a mild degree of differential rotation. Here, dynamically stable models exist, as shown in [8]. Given the fact that the stars of this EOS resemble quark stars, we conjecture that stable ergostars of quark or strange matter will have more favorable possibilities for exist-

tence. When a causal core is found deep in the high density regime of a neutron star, the number of ergostars that we were able to construct diminished.

V. ACKNOWLEDGMENTS.

This work was supported by National Science Foundation Grant No. PHY-1662211 and the National Aeronautics and Space Administration (NASA) Grant No. 80NSSC17K0070 to the University of Illinois at Urbana-Champaign. This work

made use of the Extreme Science and Engineering Discovery Environment, which is supported by National Science Foundation Grant No. TG-MCA99S008. This research is part of the Blue Waters sustained-petascale computing project, which is supported by the National Science Foundation (Grants No. OCI-0725070 and No. ACI-1238993) and the State of Illinois. Blue Waters is a joint effort of the University of Illinois at Urbana-Champaign and its National Center for Supercomputing Applications. Resources supporting this work were also provided by the NASA High-End Computing Program through the NASA Advanced Supercomputing Division at Ames Research Center.

-
- [1] B. P. Abbott *et al.* (Virgo, LIGO Scientific), *Phys. Rev. Lett.* **119**, 161101 (2017), arXiv:1710.05832 [gr-qc].
- [2] V. Savchenko *et al.*, *Astrophys. J.* **848**, L15 (2017), arXiv:1710.05449 [astro-ph.HE].
- [3] V. Savchenko *et al.*, GCN Circular No. 21507, 2017.
- [4] K. S. Thorne, R. H. Price, and D. A. Macdonald, *The Membrane Paradigm* (Yale University Press, New Haven, 1986).
- [5] S. S. Komissarov, *Mon. Not. Roy. Astron. Soc.* **350**, 407 (2004), arXiv:astro-ph/0402403.
- [6] S. S. Komissarov, *Mon. Not. Roy. Astron. Soc.* **359**, 801 (2005), arXiv:astro-ph/0501599.
- [7] M. Ruiz, C. Palenzuela, F. Galeazzi, and C. Bona, *Mon. Not. Roy. Astron. Soc.* **423**, 1300 (2012).
- [8] A. Tsokaros, M. Ruiz, L. Sun, S. L. Shapiro, and K. Uryū, *Phys. Rev. Lett.* **123**, 231103 (2019), arXiv:1907.03765 [gr-qc].
- [9] H. Komatsu, Y. Eriguchi, and I. Hachisu, *Monthly Notices of the Royal Astronomical Society* **239**, 153 (1989).
- [10] J. L. Friedman, *Communications in Mathematical Physics* **63**, 243 (1978).
- [11] G. Moschidis, *Communications in Mathematical Physics* **358**, 437 (2018), arXiv:1608.02035 [math.AP].
- [12] N. Comins and B. Schutz, *Proceedings Of The Royal Society Of London A Mathematical And Physical Sciences* **364**, 211 (1978).
- [13] S. Yoshida and Y. Eriguchi, *Monthly Notices of the Royal Astronomical Society* **282**, 580 (1996).
- [14] R. Brito, V. Cardoso, and P. Pani, *Lect. Notes Phys.* **906**, pp.1 (2015), arXiv:1501.06570 [gr-qc].
- [15] J. R. Wilson, *Astrophys. J.* **176**, 195 (1972).
- [16] E. M. Butterworth and J. R. Ipser, *Astrophys. J.* **200**, L103 (1975).
- [17] M. Ansorg, A. Kleinwachter, and R. Meinel, *Astron. Astrophys.* **381**, L49 (2002), arXiv:astro-ph/0111080 [astro-ph].
- [18] S. L. Shapiro, *Astrophys. J.* **544**, 397 (2000).
- [19] M. D. Duez, Y. T. Liu, S. L. Shapiro, M. Shibata, and B. C. Stephens, *Physical Review Letters* **96**, 031101 (2006).
- [20] G. B. Cook, S. L. Shapiro, and S. A. Teukolsky, *Astrophys. J.* **398**, 203 (1992).
- [21] F. Douchin and P. Haensel, *Astron. Astrophys.* **380**, 151 (2001), arXiv:astro-ph/0111092.
- [22] K. Uryū, A. Tsokaros, F. Galeazzi, H. Hotta, M. Sugimura, K. Taniguchi, and S. Yoshida, *Phys. Rev.* **D93**, 044056 (2016).
- [23] H. Komatsu, Y. Eriguchi, and I. Hachisu, *Mon. Not. Roy. Astron. Soc.* **237**, 355 (1989).
- [24] J. S. Read, B. D. Lackey, B. J. Owen, and J. L. Friedman, *Phys. Rev.* **D79**, 124032 (2009).
- [25] P. Haensel and J. L. Zdunik, *Nature (London)* **340**, 617 (1989).
- [26] J. M. Lattimer and M. Prakash, *Phys. Rept.* **621**, 127 (2016).
- [27] J. L. Friedman, J. R. Ipser, and R. D. Sorkin, *Astrophys. J.* **325**, 722 (1988).
- [28] K. Takami, L. Rezzolla, and S. Yoshida, *Mon. Not. Roy. Astron. Soc.* **416**, L1 (2011), arXiv:1105.3069 [gr-qc].
- [29] J. D. Kaplan, C. D. Ott, E. P. O'Connor, K. Kiuchi, L. Roberts, and M. Duez, *Astrophys. J.* **790**, 19 (2014), arXiv:1306.4034 [astro-ph.HE].
- [30] A. Bauswein and N. Stergioulas, *Mon. Not. Roy. Astron. Soc.* **471**, 4956 (2017), arXiv:1702.02567 [astro-ph.HE].
- [31] L. R. Weih, E. R. Most, and L. Rezzolla, *Mon. Not. Roy. Astron. Soc.* **473**, L126 (2018), arXiv:1709.06058 [gr-qc].
- [32] N. Stergioulas and J. Friedman, *Astrophys. J.* **444**, 306 (1995), arXiv:astro-ph/9411032 [astro-ph].
- [33] M. Ansorg, D. Gondek-Rosiska, and L. Villain, *Monthly Notices of the Royal Astronomical Society* **396**, 23592366 (2009).
- [34] P. L. Espino, V. Paschalidis, T. W. Baumgarte, and S. L. Shapiro, *Phys. Rev.* **D100**, 043014 (2019), arXiv:1906.08786 [astro-ph.HE].
- [35] M. Shibata, T. W. Baumgarte, and S. L. Shapiro, *The Astrophysical Journal* **542**, 453 (2000).
- [36] T. W. Baumgarte, S. L. Shapiro, and M. Shibata, *Astrophys. J.* **528**, L29 (2000), arXiv:astro-ph/9910565 [astro-ph].
- [37] A. Tsokaros, M. Ruiz, S. L. Shapiro, L. Sun, and K. Uryū, *Phys. Rev. Lett.* **124**, 071101 (2020), arXiv:1911.06865 [astro-ph.HE].
- [38] M. Ruiz, S. L. Shapiro, and A. Tsokaros, *Phys. Rev.* **D98**, 123017 (2018), arXiv:1810.08618 [astro-ph.HE].
- [39] M. Ruiz, R. N. Lang, V. Paschalidis, and S. L. Shapiro, *Astrophys. J.* **824**, L6 (2016).
- [40] V. Paschalidis, M. Ruiz, and S. L. Shapiro, *Astrophys. J. Letters* **806**, L14 (2015).
- [41] K. Uryū, A. Tsokaros, L. Baiotti, F. Galeazzi, K. Taniguchi, and S. Yoshida, *Phys. Rev.* **D96**, 103011 (2017), arXiv:1709.02643 [astro-ph.HE].